Journal of Biomedical Optics

BiomedicalOptics.SPIEDigitalLibrary.org

Optical model of the murine lung to optimize pulmonary illumination

Madeleine S. Durkee
Fatemeh Nooshabadi
Jeffrey D. Cirillo
Kristen C. Maitland

SPIE.

Madeleine S. Durkee, Fatemeh Nooshabadi, Jeffrey D. Cirillo, Kristen C. Maitland, "Optical model of the murine lung to optimize pulmonary illumination," *J. Biomed. Opt.* **23**(7), 071208 (2018), doi: 10.1117/1.JBO.23.7.071208.

Optical model of the murine lung to optimize pulmonary illumination

Madeleine S. Durkee,[a] Fatemeh Nooshabadi,[a] Jeffrey D. Cirillo,[b] and Kristen C. Maitland[a,*]
[a]Texas A&M University, Department of Biomedical Engineering, College Station, Texas, United States
[b]Texas A&M Health Science Center, Department of Molecular Pathogenesis and Immunology, Bryan, Texas, United States

Abstract. We describe a Monte Carlo model of the mouse torso to optimize illumination of the mouse lung for fluorescence detection of low levels of pulmonary pathogens, specifically *Mycobacterium tuberculosis*. After validation of the simulation with an internally illuminated optical phantom, the entire mouse torso was simulated to compare external and internal illumination techniques. Measured optical properties of deflated mouse lungs were scaled to mimic the diffusive properties of inflated lungs *in vivo*. Using the full-torso model, a 2× to 3× improvement in average fluence rate in the lung was seen for dorsal compared with ventral positioning of the mouse with external illumination. The enhancement in average fluence rate in the lung using internal excitation was 40× to 60× over external illumination in the dorsal position. Parameters of the internal fiber optic source were manipulated in the model to guide optimization of the physical system and experimental protocol for internal illumination and whole-body detection of fluorescent mycobacteria in a mouse model of infection. [DOI: 10.1117/1.JBO.23.7.071208]

Keywords: tissue optics; optical phantom; Monte Carlo simulation; bacteria; lung; intravital illumination.

Paper 170635SSRR received Oct. 2, 2017; accepted for publication Mar. 1, 2018; published online Mar. 23, 2018.

1 Introduction

Tuberculosis, the disease caused by *Mycobacterium tuberculosis* (Mtb), is now classified as the deadliest infectious disease caused by a single organism, surpassing HIV in the annual number of fatalities in 2014.[1] This epidemic is a multifaceted problem; there are limitations of current diagnostic methods and emergence of multidrug resistant and extensively drug-resistant strains.[2–4] In addition to these clinical problems, the disease has a complex, multistage pathogenesis in humans, the progression of which is not fully understood or completely agreed upon in the scientific community.[5] Animal models are used to study Mtb, with nonhuman primates serving as one of the best models for pathogenesis.[6] However, small animal models such as the mouse and guinea pig are more cost-effective and are important models for clinically relevant studies on therapy response.[7,8] While most studies rely on sacrifice at discrete time points to achieve data on therapy response,[9,10] optical techniques show promise in improving detection of bacteria in small animal models of disease.

Whole-animal imaging is a powerful tool to measure biological fluorescence and bioluminescence *in vivo*; however, the thickness of tissue that the optical excitation and emission must traverse leads to low sensitivity for optical targets located deep within the body.[11] A small animal whole-body imaging system using epi- or transillumination [Figs. 1(a) and 1(b)] has been employed to detect a tdTomato-expressing strain of mycobacteria (bacillus Calmette–Guerin—BCG) or Mtb-specific near-infrared (NIR) reporter enzyme fluorescence (REF) probes *in vivo* in a mouse model.[12–15] These external illumination methods allow for longitudinal studies but, unfortunately, suffer from a relatively high detection threshold compared with physiologically relevant infectious doses of 1 to 10 bacteria.[16] A pulmonary bacterial load of 10^5 colony forming units (CFU) or higher is needed to effectively detect the signal. This high detection threshold limits these methods when determining therapeutic efficacy of antimicrobials for pathogenic bacteria. Recently, a microendoscope (ME) has been incorporated into the animal imaging system as an alternate illumination source to more effectively deliver the higher energy excitation light into the lung of the animal where the bacterial fluorescent target resides [Fig. 1(c)]. This addition to the imaging system improves the detection threshold by orders of magnitude.[17,18]

The sensitivity of whole-animal fluorescence imaging is also dependent on animal position. Figure 2 shows the irradiance collected from infected mice, including signal, tissue autofluorescence, and any source leakage. External illumination suffers from a high detection threshold at both ventral and dorsal positions. Fluorescence detection with internal illumination is also position dependent, with the dorsal position having an improved signal–to-noise ratio.[18] Whether these differences stem from ineffective illumination of the lung or a limitation of collecting fluorescence signal is unknown, but this knowledge is integral to optimization of the imaging system for detection of low bacteria levels. A three-dimensional (3-D) model of animal illumination will help to explain differences in both the light source and animal position in effectively coupling excitation light into the lung where the bacteria reside.

Radiative transport models, specifically Monte Carlo simulations, are a powerful tool in quantifying the photon flux within biological tissue to help with optimizing medical and biological imaging techniques.[19,20] These models are a stochastic version of the radiative transport equation (RTE) in which the optical properties of the material—in this case,

*Address all correspondence to: Kristen C. Maitland, E-mail: kmaitland@tamu.edu

1083-3668/2018/$25.00 © 2018 SPIE

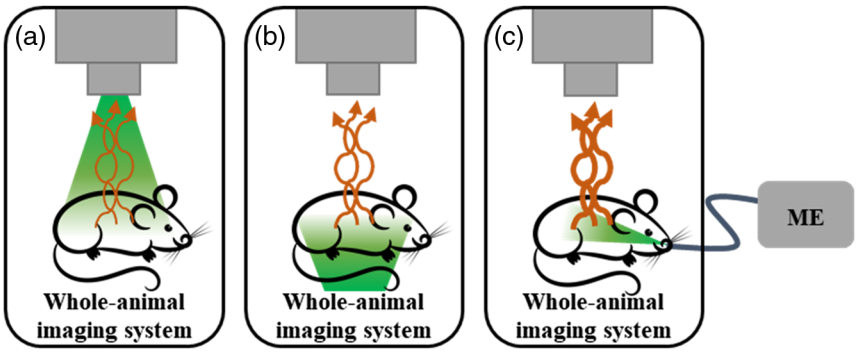

Fig. 1 Fluorescence whole-animal imaging of mice can be accomplished through multiple illumination pathways including (a) external epi-illumination, (b) external transillumination, and (c) internal illumination with an ME light source.

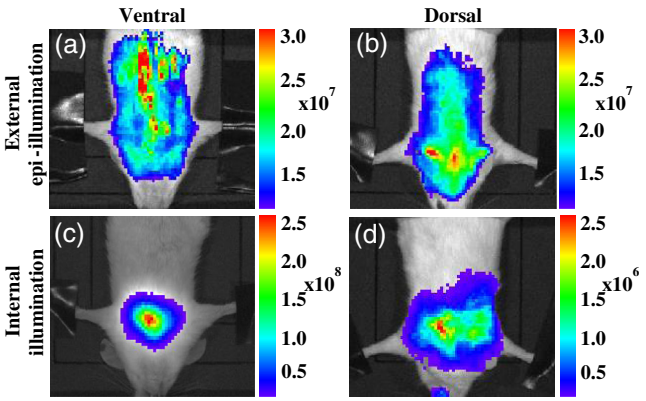

Fig. 2 Position of the mouse in the imaging system effects collected fluorescence. Mice were intratracheally infected with 10^6 colony forming units BCG and administered REF substrate 24 h postinfection. Fluorescence distribution is different with external epi-illumination in (a) the ventral and (b) dorsal positions. Under the same infection conditions, detected fluorescence intensity with internal illumination also varies for mice imaged in (c) the ventral and (d) dorsal positions. Although the fluorescence signal is higher in (c) the ventral position, the signal-to-noise ratio was found to be significantly higher for (d) the dorsal position.[18] All radiance values are measured in photons/s/cm^2/steradian.

biological tissue—determine the path of a photon through that material. Therefore, an accurate solution to the RTE can be generated with a sufficiently high photon count. The scope of the application of Monte Carlo methods to biological systems has been expanded to represent complex, 3-D biological structures, ranging from cutaneous blood vessels to a whole-mouse model, using a variety of methods including voxelated models and triangulated meshes.[21–26]

We are primarily interested in light transport within the lung as the predominant organ affected by tuberculosis. However, to compare the effects of external illumination and different animal positions with internal illumination with a fiber optic source, we must also simulate the torso of the animal and other organs that may have a significant effect on delivery of excitation light to fluorescent targets within the lung. LightTools (Synopsys, Inc.) illumination software uses the Monte Carlo method to track photons through free space and turbid media. This software has been used to model radiative transport in multilayer epithelial models[27] and in a more complex whole-finger model for the design of a ring pulse oximeter.[28] For the purposes of designing a full-torso mouse model with external and internal illumination, the airway is a primary component of our illumination model. A solid model of the airway was imported into LightTools for the illumination model. The model described below compares various strategies of external and internal illumination of a mouse torso, including airway, lung, heart, and other soft tissues, to determine the optimal illumination strategy for sensing fluorescent bacteria or a bacteria-sensing probe at a low bacterial load in a live mouse. The system is modeled at visible and NIR wavelengths to account for fluorescence from genetically modified bacteria (visible) and the bacteria-sensing fluorogenic probe (NIR).[17,18] Rapid evaluation of modifications to the internal illumination system, including addition of a light diffuser tip, positioning of the fiber source within the airway, and modified divergence angle of the fiber source, are enabled by the computational model without the need for extensive animal experiments.

2 Methods

In the development of a computer model to simulate light transport in the mouse lung, a simplified physical lung phantom was first designed to validate the computational model. Optical properties of excised mouse lung tissue were experimentally measured and used as inputs into the simplified model and phantom design. The validation model consisted of a block tissue phantom with the optical properties of a deflated mouse lung and a mesoscale, simplified airway. Once validated with imaging of the phantom, a more complex and anatomically representative airway, lung, and torso structure was generated in the computer model. Various illumination configurations were tested using this model. All Monte Carlo simulations (validation studies and the advanced model) were completed using LightTools Illumination software on a personal desktop computer (6 core Intel i7 processor, 3.3 GHz, 72 GB RAM).

2.1 *Measured Optical Properties of Mouse Lung*

Optical properties of Mtb-infected mouse lung were measured experimentally to provide inputs into the computational and physical models. All animal experiments were approved by Texas A&M University Institutional Animal Care and Use Committee. Mice were infected by intratracheal instillation of 10^6 CFU BCG. After 24 h of infection, mice were sacrificed, and the lungs were immediately excised. The excised lungs were placed in a well between two microscope slides. This well was created by curing a ~1.5 mm layer of polydimethylsiloxane

Table 1 Absorption coefficients (μ_a) and reduced scattering coefficients (μ_s') of infected mouse lung and validation phantoms at wavelengths of interest. Percent error between total flux measured experimentally with the phantom and simulated in the model.

Measured infected, deflated mouse lung tissue		
Wavelength (nm)	μ_a (cm^{-1})	μ_s' (cm^{-1})
535	5.99 ± 1.92	43.5 ± 14.6
730	1.06 ± 0.49	35.2 ± 11.7

Phantom properties and validation results			
Phantom 535 (nm)	μ_a (cm^{-1})	μ_s' (cm^{-1})	Error (%) of simulation v. phantom
535	4.53	67.4	4.59%
730	3.75	52.1	4.40%
Phantom 730 (nm)	μ_a (cm^{-1})	μ_s' (cm^{-1})	Error (%) of simulation v. phantom
535	2.22	44.5	3.66%
730	1.75	35.3	2.86%

(PDMS) on a single microscope slide and using a custom biopsy punch to remove a 15-mm diameter section. Lungs were not sliced into thin sections because the organ had to be homogenized and plated for culture to quantify bacterial load. Lung reflectance and transmittance were measured at 535 and 730 nm wavelengths using an integrating sphere. The reduced scattering and absorption coefficients of excised mouse lungs were estimated using inverse adding-doubling method after collection of reflectance and transmittance values.[29] The resulting optical properties assume that the lungs remain well perfused and are fully deflated. Table 1 shows the optical properties of infected mouse lung for the two excitation wavelengths of interest: 535 nm for tdTomato fluorescent protein and 730 nm for REF substrate CNIR800.[17,18] Measured optical properties for the infected mouse lung are in the range of healthy human and piglet lung tissue optical properties in the literature.[30,31]

2.2 *Airway and Lung Phantom*

Optical phantoms were created from PDMS with India ink and titanium dioxide (TiO_2) to replicate the measured absorbing and scattering properties of lung tissue, respectively. Two separate phantoms were created to simulate the optical properties of the tissue at the two wavelengths of interest (Table 1). Phantom 535 contains 3 mg TiO_2 and 7.5 μL India ink per gram of PDMS and approximates infected lung measured at 535 nm. Phantom 730 contains 2 mg TiO_2 and 3.5 μL India ink per gram of PDMS and models the infected lung at 730 nm. Both phantoms were imaged at both illumination wavelengths to provide additional validation data for the computer model.

Structurally, the lung has a unique surface for internal illumination through the trachea. On the mesoscale, the airway branching results in a complex air–tissue interface where a stark contrast in refractive index between air and tissue will affect the transport of photons within the organ. The airway was included in both the computational and physical models of the physiological system to better evaluate the accuracy of the simulation to a biological environment. A fractal tree mock-airway was designed and printed out of a base-soluble material as an internal mold for the PDMS airway phantom. The preliminary structure shown in Fig. 3(a) was designed to be easily 3-D-printed in-house on a fused deposition modeling printer (Stratasys®, Fortus360mc). This soluble structure was secured in a rectangular mold for pouring the PDMS and optical particle mixture. Upon curing, the mock airway was dissolved out of the phantom, leaving an airway void and a pathway for internal illumination of the solid rectangular block phantom. This method of incorporating complex geometry into a silicone matrix has previously been employed for designing flow systems for surgical training.[32] 3-D printing is also becoming a popular method for fabricating phantom molds and for manufacturing the phantoms themselves.[33–35] The phantom fabrication methods used here are described in full detail by Durkee et. al.[36]

2.3 *Phantom Imaging*

Imaging of the lung phantoms was performed in an IVIS Lumina II (PerkinElmer) whole-animal optical imaging system to validate the computer simulation of the analogous simplified model. For internal illumination, the IVIS illumination pathway was blocked, and a fiber ME light source was inserted into the airway void until the tip was in contact with the wall at the bifurcation.[37] The ME output power was set at 1 μW for

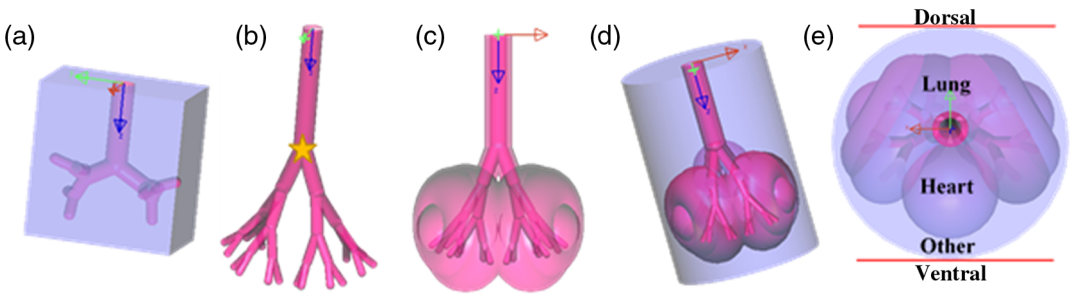

Fig. 3 (a) 3-D models for photon transport in LightTools. The rectangular phantom used for validation studies has a four-generation fractal tree as a model airway. (b) The full-torso model of the mouse includes a more anatomically accurate model airway and lungs of comparable volume to that of a mouse. (d, e) The lung and heart are immersed in a cylindrical model of other soft tissues. The star in (b) is the location of the internal illumination source.

both wavelengths. The IVIS emission filter wheel was set to "open" to collect the illumination light, and camera settings were set to automatic exposure. Total irradiance of the top surface of a phantom measured by the IVIS imaging system was compared with the simulation for 535- and 730-nm illumination studies.

2.4 *Mouse Torso Model*

Once the simulation was validated using the simplified phantom, the airway structure within the simulation was updated to be more representative of the largest branches of the murine airway [Fig. 3(b)] based on computed tomography (CT) images.[38,39] The simulated lung was designed around the airway [Fig. 3(c)], with the general anatomy and size constraints of the mouse lung modeled after similar CT images.[39,40] *In vivo*, the lung is a dynamic and porous organ that scatters light much more effectively than solid tissue. Within the computational model, the lung properties can be adapted from the measured values of deflated lung to represent inflated lung at different points in the respiratory cycle. Here, we optimize the computational model to represent a point in the cycle indicative of passive respiration to analyze the illumination performance of external and internal illumination sources. The heart and other soft tissues are also represented [Figs. 3(d) and 3(e)] to more effectively model external illumination and to address photons scattered into the lung after traversing other tissues.

2.5 *Simulated Optical Properties of Inflated Lung*

The optical properties of the lung were measured after excision, assuming the organ was deflated. In a living mouse, the lung will always have some level of inflation, with air making up at least 30% of the organ volume after expiration and up to 90% of the organ volume after inspiration.[41,42] The simulated optical properties can be mathematically manipulated to represent the scattering and absorption of an inflated lung, based on the optical properties of the deflated lung, and the alveolar size and density.[30]

For this model, we assumed a constant alveolar diameter of 55 μm.[43] Alveoli were assumed to be spherical in the calculation of the volume of a single alveolus, V_{alveolus}. A number density of alveoli were calculated based on mouse lung characteristics. First, because we have a static model, we assumed a constant level of inflation with air composing 80% of the organ volume. Using this inflation factor, f_i, and the properties listed in Table 2, the number of alveoli in the lung was calculated using

$$N_{\text{alveoli}} = f_i \frac{V_{\text{lung}}}{V_{\text{alveolus}}}. \tag{1}$$

The alveolar density

$$\rho_{\text{alveoli}} = \frac{N_{\text{alveoli}}}{V_{\text{lung}}}, \tag{2}$$

was calculated to be 9195 alveoli/mm^3. The alveolar density was used to find the new reduced scattering coefficient, μ_s', of the inflated lung

$$\begin{aligned}\mu'_{\text{s lung}} &= \mu'_{\text{s tissue}} + \mu'_{\text{s alveoli}},\\ &= \mu'_{\text{s tissue}} + [\rho_{\text{alveoli}}\sigma_s(1 - g_{\text{alveoli}})],\end{aligned} \tag{3}$$

(adjusted from Ref. 30), where $\mu'_{\text{s tissue}}$ was measured from the deflated tissue. Treating the alveoli as scatterers dispersed in lung tissue, the radius and refractive index of the alveoli allow the alveolar cross section to be used as the scattering cross section (σ_s) as the alveoli fall into the regime of geometric optics.[44] The anisotropy factor, g, of the alveoli was estimated at 0.6.[30] The resulting reduced scattering coefficients (μ_s') and mean free paths (MFP $= 1/\mu_s'$) are comparable to that of liquid foams with a similar liquid fraction to the air-tissue ratio used in the lung.[45,46]

The absorption coefficient, μ_a, of inflated lung was also adjusted because the path length available for absorption changes significantly with air in the tissue.[30] For the level of static inflation assumed in this model, only 20% of the total lung volume, V_{lung}, is actually tissue, V_{tissue}. With no absorption occurring in the air-space, the absorption coefficient is reduced accordingly by this factor,

$$\mu_{a,\text{ lung}} = \mu_{a,\text{tissue}} \frac{V_{\text{tissue}}}{V_{\text{lung}}}. \tag{4}$$

Table 2 Properties of inflated mouse lung used to calculate approximate optical properties.

Inflated lung characteristics		
Property	Value(s) in literature	Value used in model
Lung volume at max inspiration (mm^3)	1000 to 1500[38,43,47]	1060
Lung tissue volume (mm^3)	100 to 200[42,48]	212[a]
Alveolar diameter (μm)	35 to 75[49,50]	55

Lung optical properties				
Wavelength (nm)	Deflated μ_a (cm^{-1})	Deflated μ_s' (cm^{-1})	Inflated μ_a (cm^{-1})	Inflated μ_s' (cm^{-1})
535	5.99	43.57	1.20	130.84
730	1.07	35.27	0.21	122.54

[a]Lung tissue volume was calculated from lung volume and an inflation factor of 0.8.

2.6 *Heart and Other Soft Tissues*

The heart is important in this simulation because of its high blood content and, therefore, high absorption in the visible range. While a majority of the photons contributing to the illumination profile of the lung come directly from the internal source, some fraction of the light will escape into the surrounding tissue. The properties of that tissue, including the heart, will determine how much the illumination of the lung is affected by its surroundings. The heart is assumed to be mainly an absorber, and the optical properties of partially oxygenated blood are used for the heart in this model (Table 3).[51] The remaining tissue includes muscle, fat, skin, and bone; however, bone is not included in this model for simplicity. Overall optical properties for the collective "other soft tissues" are estimated based on values from the literature[31] and are listed in Table 3. These values were used to determine the MFP and transmissivity (T) as inputs for the heart and other soft tissue materials. LightTools was set to interpolate values to determine the properties of material at wavelengths within the range listed in Table 3. If a wavelength simulated was out of the range listed, the value closest to that wavelength is used. For example, the optical properties of the heart at 535 nm were identical to those listed at 665 nm in Table 3.

Table 3 Optical properties for other soft tissues from Ref. 30.

Wavelength (nm)	μ_a (cm^{-1})	μ_s' (cm^{-1})
Epidermis		
514	3.0	58[a]
585	3.0	41[a]
800	2.3	30[a]
Dermis		
514	4.4	139[a]
585	3.6	99[a]
800	4.0	62[a]
Subcutaneous fat		
520	4.4	33.1
570	3.1	28.9
820	1.0	19.8
Muscle		
633	1.21	8.9
900	0.32	5.9
Calculated properties for "other soft tissues"		
514	1.84	17.19
585	1.70	16.33
800	0.644	10.96
Heart		
665	12.37	6.23
960	4.97	4.04

[a]Values were calculated from scattering coefficient and anisotropy factor. Values from LightTools biological materials library were used for heart optical properties.

2.7 *Illumination and Detection Parameters*

The fiber bundle ME used for internal illumination has a divergence half angle of 20.5 deg, and experimental protocol specifies that the endoscope should be in contact with the tissue for imaging. This internal source was modeled as a point source with a divergence half angle of 20.5 deg to mimic the fiber bundle used in imaging experiments.[17,18] To model epi-illumination within the whole-body imaging system, dorsal and ventral external illumination sources were placed 20 mm away from the simulated phantom or torso and uniformly illuminated a plane located at the surface nearest to that source. Validation simulations were run with 1e6 photons with a source power of 1 μW. All simulations of the mouse torso model were run in triplicate with 1e5 photons. External illumination simulation times ranged from 30 to 45 min, and internal illumination simulation times ranged from 3.5 to 4 h depending on source wavelength. External and internal sources at both wavelengths were set to 1 mW total power emitted.

Illumination of the lung was analyzed using average fluence rate in the lung and source efficiency, defined as average fluence rate in the lungs relative to average fluence rate in the entire simulated torso. Detection planes parallel to the coronal plane were placed at 0.5 mm intervals through the solid model of the torso to directly record photon flux, with bins of 0.1 mm $\times$ 0.1 mm in each collection mesh. The complete detection matrix is $200 \times 250 \times 35$ elements, corresponding to a total of 1.75e6 elements (8750 mm^3).

Spatial distribution of the light within the lung was analyzed by fitting the average fluence rate in the detection planes to the exponential curve

$$f(x) = a * e^{-bx}, \tag{5}$$

where a is the average fluence rate nearest the source and b is the decay constant. For external illumination, a is calculated at the ventral or dorsal plane, and, for internal illumination, a is calculated at the plane intersecting the internal source. Therefore, these decay curves move across the body for external illumination and from the source outward for internal illumination. To quantitatively compare different sources, an average fluence rate for the entire lung was calculated from the collection matrix by masking each detection plane with the intersecting lung geometry. The fluence rates from the masked data were averaged over the collection matrix to get an average fluence rate within the lung. The computational model of the mouse torso was used to evaluate (1) internal and external illumination, including ventral and dorsal positioning of the mouse; (2) the addition of a diffuser tip for radial illumination from the internal source; (3) positioning of the internal illumination source relative to the tracheal bifurcation; and (4) divergence angle of the optical fiber output.

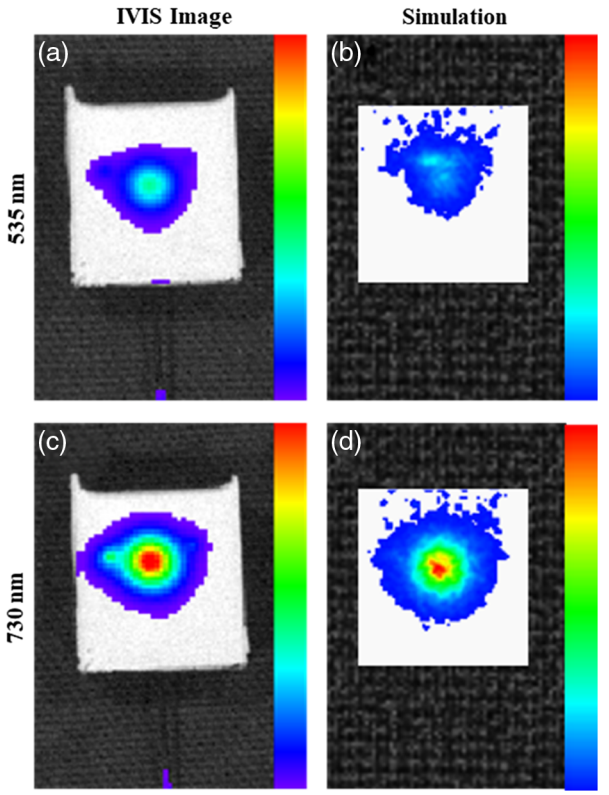

Fig. 4 Validation of the computational model with IVIS imaging of optical phantoms shows a similar irradiance profile at the phantom surface. Phantom 535 is shown here illuminated internally with (a) 535 nm and (c) 730 nm ME sources. The simulation replicates total flux output to the detector (Table 1) and the irradiance profile at (b) 535 and (d) 730 nm.

3 Results

3.1 *Validation of Computer Model with Lung Phantom Imaging*

The measured optical properties of the phantoms and the accuracy of the simulation to reproduce the experimental IVIS imaging results are shown in Table 1. The simulation was able to replicate the total photon flux within 5.0% for both phantoms at both wavelengths. Figure 4 also demonstrates a similar irradiance profile between phantom imaging and the computational model for both wavelengths. After verifying agreement between the computational and physical models, we expanded on the computational model to better mimic the murine anatomy, as shown in Fig. 3. All results following verification are from this advanced model.

3.2 *External Illumination Versus Internal Illumination*

As described earlier, the position of the mouse relative to an external illumination source has an effect on the signal collected from a fluorescent target within the lung. The 3-D illumination of the lung was analyzed for external illumination from the dorsal and ventral sides and for internal illumination. An internal source in contact with the tissue with a divergence half angle of 20.5 deg was used for the comparison between internal and external illumination.

Figure 3(e) shows a transverse view of the optical model, with the dorsal and ventral sides indicated. The asymmetry between dorsal and ventral causes a difference in the illumination profile of the lung [Figs. 5(a)–5(b) and 5(d)–5(e)]. Both positions yield an exponential decay in fluence rate with depth in the lung [Fig. 5(g)]. The decay constant, b, varies for both orientation of the external source and wavelength ($p < 0.0001$) according to a comparison of fits of a nonlinear regression for each illumination strategy (Table 4). The difference in penetration depth of external illumination is most drastically affected by the heart, the main organ between the source and the lung in the ventral position. As a highly absorbing organ (due to blood content), the heart prevents a portion of the illumination from reaching the lungs, resulting in a lower a parameter in the corresponding decay equations in Table 4.

Internal illumination avoids the problem of traversing other tissues, and minimal light is lost to surrounding tissue. The illumination still decays exponentially with distance from the light source [Fig. 5(h), Table 4], but the efficiency of the light source at coupling light into the lung is much higher (>60%), compared with less than 10% efficiency for either external illumination orientation at either wavelength (Table 5). The average fluence rate in the lung with the internal source is also significantly higher than external illumination when the sources have equal power ($p \ll 0.0001$).

3.3 *Diffusing Fiber Internal Illumination Source*

Simulations and previous animal experiments indicate that internal illumination is more efficient than external illumination in either position. To estimate the potential for further improvement in illumination of the lung, modifications to the internal source were designed and tested with the optical model. First, a 5-mm-long cylindrical light diffuser design was simulated [Fig. 6(a)]. Diffusing fibers can be designed to preferentially emit light radially or out the distal end of the diffuser.[52] The percentage of power emitted from the distal end of the diffuser relative to the homogeneous radial emission along the length of the diffuser was varied from 10% to 100%. 100% power emitted from the tip of the diffuser is equivalent to the ME condition. All simulations were performed with the diffusing fiber tip in contact with the tissue at the tracheal bifurcation. As less power was emitted along the length of the diffuser, the efficiency of the source at coupling light into the lung increased, along with average fluence rate in the lung. Trends in efficiency and average fluence rate were similar across both wavelengths of interest [Figs. 6(d) and 6(g)].

3.4 *Positioning of Fiber Internal Illumination Source*

The original internal source modeled off the ME specifications was simulated at different positions within the trachea to determine the effect of source placement on the illumination of the lung [Fig. 6(b)]. Starting with the internal source in contact with the tissue at the tracheal bifurcation (0 mm), the endoscope was moved away from the tissue surface, up to 6 mm offset, effectively pulling the endoscope out of the airway. As the internal source was moved away from the tracheal bifurcation [Fig. 6(e)], the efficiency increased moderately ($p \ll 0.0001$) until peaking near 2 mm distance from the bifurcation, then decreased below the initial efficiency at the tissue surface. In the region where efficiency hit a maximum, the simulation also indicated a maximum fluence rate within the lung [Fig. 6(h)].

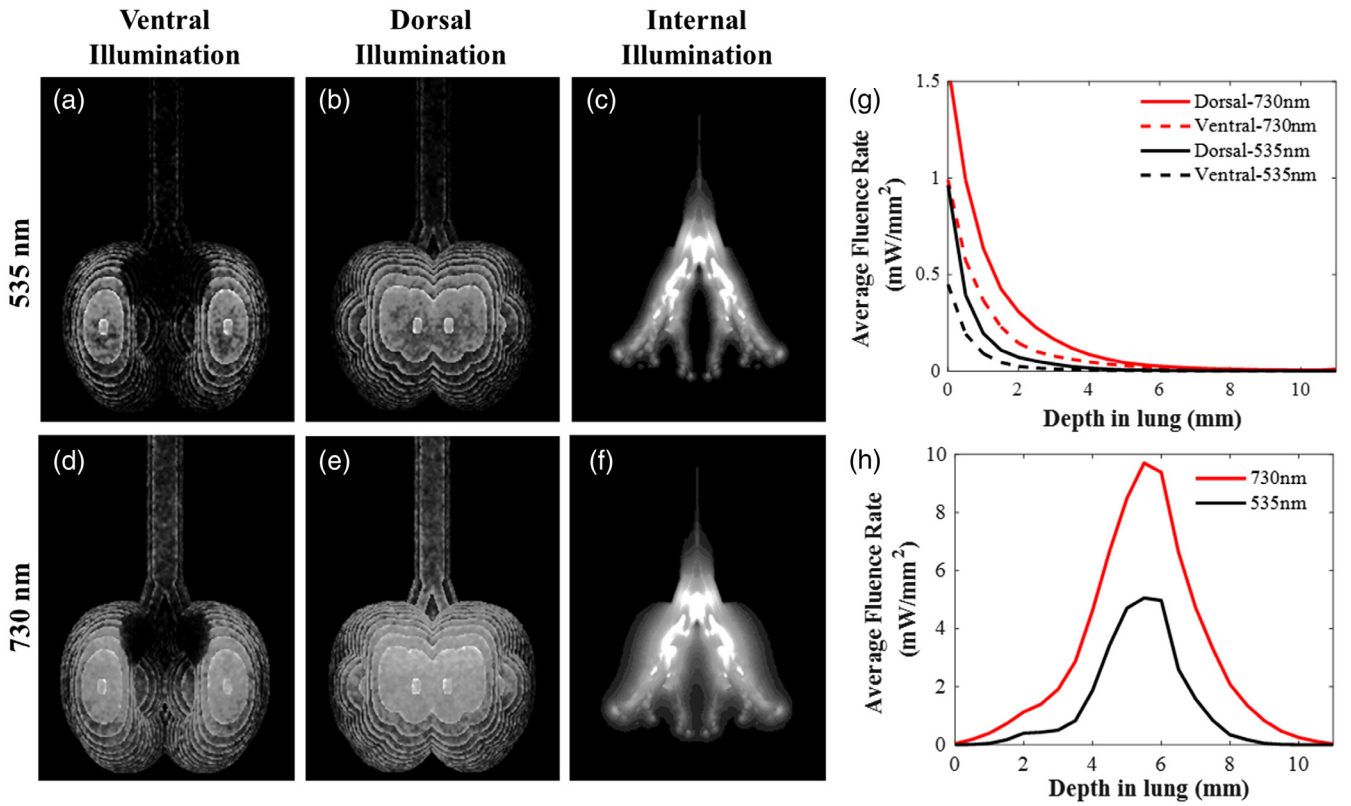

Fig. 5 (a, d) Maximum intensity projections of the light distribution within the lung are shown for external illumination from the ventral side of the mouse, (b, e) external illumination from the dorsal side of the mouse, and (c, f) internal illumination. (a–c) A difference in penetration can be seen between the excitation wavelength for tdTomato and (d–f) the excitation wavelength for the REF NIR probe. All projections with epi-illumination are normalized to have the same maximum. In the internal illumination projections, all values above that maximum are set to that maximum to better represent the average fluence rate on the same scale. The average fluence rate within the lung decreases exponentially with distance away from the source for both (g) external illumination and (h) internal illumination. However, (g, h) the average fluence rate is higher throughout the lung with internal illumination.

Table 4 Decay of fluence rate within lung. Average power was fit to a decaying exponential: $f(x) = a * \exp(-b * x)$, where a is the initial average fluence rate at the detection plane nearest the source and b is the decay constant.

External illumination (decay from lung surface inward)	Initial average fluence rate (mW/mm^2) (a)	Decay constant (b)	R^2
Dorsal-535 nm	0.9546	1.642	0.9958
Ventral-535 nm	0.4476	1.631	0.999
Dorsal-730 nm	1.563	0.8641	0.9978
Ventral-730 nm	0.9782	0.997	0.9977
Internal illumination (decay from trachea outward)	**Initial average fluence rate (mW/mm^2) (a)**	**Decay constant (b)**	**R^2**
Trachea → dorsal side-535 nm	4.948	1.194	0.9985
Trachea → ventral side-535 nm	4.874	0.9384	0.9852
Trachea → dorsal side-730 nm	9.476	0.6618	0.999
Trachea → ventral side-730 nm	8.785	0.6207	0.9936

3.5 *Divergence Angle of Fiber Internal Illumination Source*

The final source manipulation simulated was the change of the divergence angle of the fiber bundle source [Fig. 6(c)]. The effects of the divergence angle on illumination were simulated for angles above and below the current design (20.5-deg half angle). The simulation results show an upward trend with increasing angle [Figs. 6(f) and 6(i)], with a slope of 0.021 and 0.039 μW/mm^2/deg divergence for NIR and visible wavelengths, respectively ($R^2 > 0.90$).

3.6 *Optimal Parameters of Internal Source*

Illumination of the mouse lung was improved by independently changing the location and divergence of the internal source. The optimal source placement and optimal angle were combined to further improve the lung illumination. To find the optimal illumination, a divergence half angle of 40 deg and source locations of 0.7 and 1.7 mm away from the tracheal bifurcation were selected as inputs for the optical model. While these simulations show an improved illumination over the current experimental design, the optimal internal source parameters were achieved at the original 20.5-deg divergence half angle with the source

Table 5 Ability of different illumination sources to couple light into the lung.

Illumination	Efficiency at 535 nm (%)	Average fluence rate at 535 nm (μW/mm^2)	Efficiency at 730 nm (%)	Average fluence rate at 730 nm (μW/mm^2)
External-dorsal	3.14	0.064	2.77	0.20
External-ventral	1.05	0.020	1.21	0.089
Internal	66.66	3.8	76.92	8.9

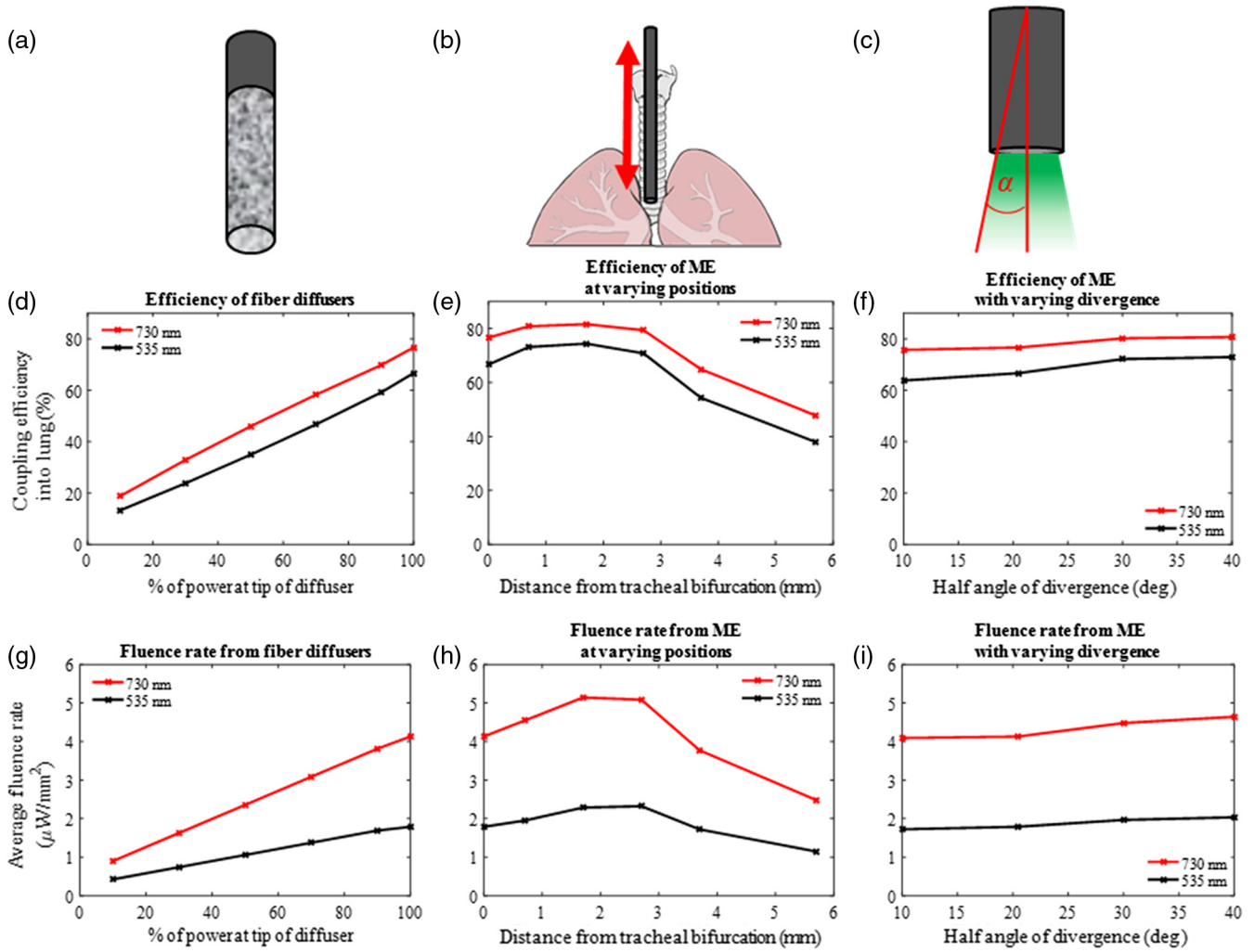

Fig. 6 The fluence rate in the lung is sensitive to the parameters of the internal source, including (a) diffuser tip, (b) fiber position, and (c) divergence angle of the fiber. The efficiency of a fiber diffuser increases as more source power is emitted through the tip of the fiber rather than radially (d). The ME efficiency is more sensitive to (e) position than (f) divergence angle. (g–i) The average fluence rate in the lung follows similar trends to efficiency for all source manipulations.

placed 1.7 mm away from the tissue surface at the tracheal bifurcation (Table 6).

To illustrate the light distribution in the lungs, the fluence rate of each detection plane was combined into a 3-D representation of internal illumination of the lung at both wavelengths of interest. Maximum intensity projections for each orientation are shown in Figs. 7(a)–7(c) for 535 nm and Figs. 7(d)–7(f) for 730 nm illumination to describe the spatial variance in the fluence rate. Video 1 [Fig. 7(g)] of the complete rotating volumes at 535 nm (top) and 730 nm (bottom) show the dependence of fluence rate on the illumination wavelength due to the differences in optical properties.

4 Discussion

4.1 *Assumptions and Limitations of the Optical Model*

The optical simulation was designed to analyze the 3-D illumination of a complex physiological system and optimize the

Table 6 Parameters and performance of optimized internal illumination. The bolded values are represented spatially in Fig. 7.

Modified internal source parameters					
Divergence angle (deg)	20.5	40	20.5	40	40
Offset from tissue (mm)	0	0	1.7	0.7	1.7
535 nm					
Efficiency of coupling to lung (%)	66.66	72.91	**74.40**	73.24	62.90
Avg. fluence rate in lung (μW/mm^2)	3.8	4.3	**4.9**	4.7	4.4
730 nm					
Efficiency of coupling to lung (%)	76.92	81.14	**82.05**	81.28	72.30
Avg. fluence rate in lung (μW/mm^2)	8.9	10.1	**11.0**	10.8	9.5

illumination source and protocol for detection of optical targets *in vivo*. While the model is structurally and optically complex, it is important to note the assumptions and limitations of the optical model. An advanced phantom was designed to validate the ability of the optical model to replicate the boundary conditions of an internal airway and source placement within that airway. Due to manufacturing constraints, the airway modeled in the validation studies is less anatomically accurate than the airway in the full torso model. Assuming that this structural change does not affect the accuracy of the optical simulation, all tissue structure in the final model remains only an approximation of the natural anatomy.

While the porous tissue of the lung is approximated with the shifted scattering properties, in reality, the airway is continuous with the alveolar ducts and sacs. The boundary between the airway and the tissue might lead to some inaccuracy in the model, but it is assumed to be an underestimation of the diffusive properties of the lung. As the airway acts somewhat as a light guide, a continuous structure would likely yield a more uniform illumination. Unfortunately, modeling a structure of this complexity within a high-photon count Monte Carlo simulation is highly intensive computationally.

Simplifying all tissue except the lung and the heart into one bulk tissue layer might cause discrepancies in the model, particularly with the external illumination model. With fur unaccounted for on the external surface of the model, this model will overestimate the transmission of external illumination into the thoracic cavity. For internal illumination, the properties of this tissue layer have only a small effect on the illumination of the lung.

It is also important to note that both the internal and external power sources modeled are normalized to 1 mW. For animal experiments with this application, internal illumination power ranges from hundreds of microwatts to ~1.3 mW, and external illumination power is controlled by the IVIS software but can be estimated to range from milliwatts to watts depending on filters and lamp settings. The average fluence rate calculation, used as a measure for illumination, scales well with source power, and efficiency of the source will not change. Therefore, with a consistent source power of 1 mW, the results for changing source power are easily predictable. As an estimation, if we were to operate at the American National Standards Institute (ANSI) standard for maximum permissible exposure (MPE) for a collimated beam on skin, the source power would scale by this value relative to the area of incidence of the source on the tissue. The smaller area of incidence of the internal source therefore requires a lower power than the external source to fall below the ANSI standard. While neither source is actually collimated, we are using these values to demonstrate the scalability of this model. Table 7 shows these values with the internal source in contact with the tissue and the external source incident on

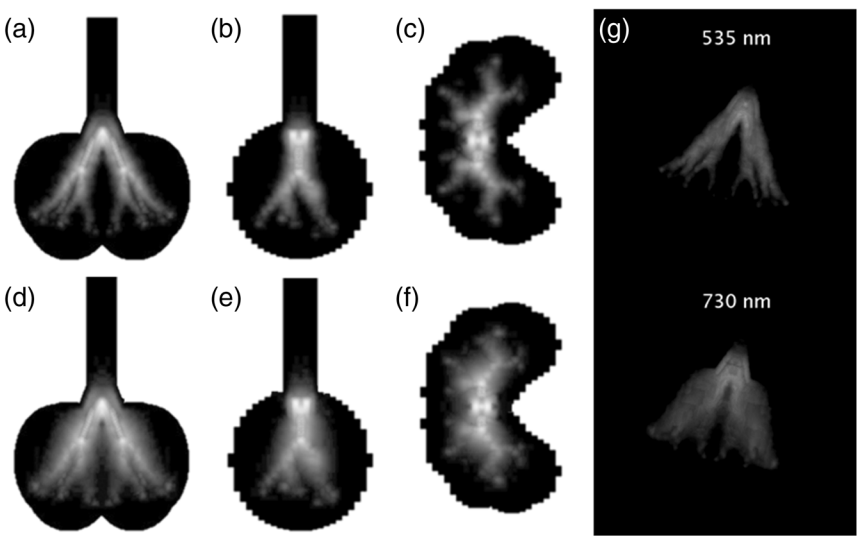

Fig. 7 The 3-D illumination in the lung is shown for (a–d) 535 nm and (e–h) 730 nm. Maximum intensity projections of the fluence rate in (a, d) the coronal plane, (b, e) sagittal plane, and (c, f) transverse plane. A mask of the lung is also shown in each projection. (g) Video of the 3-D rendering of the illumination is shown for both wavelengths (Video 1, MP4, 8.3 MB [URL: https://doi.org/10.1117/1.JBO.23.7.071208.1]).

Table 7 Values relating source power in the simulations to ANSI standards for MPE of a collimated laser beam on skin for the wavelengths of interest.

Area of incidence	
Internal source in contact with tissue	0.342 mm^2
External source	400 mm^2
535 nm	
MPE for skin	2.00 mW/mm^2
Internal source power	0.68 mW
External source power	0.68 W
730 nm	
MPE for skin	7.96 mW/mm^2
Internal source power	2.7 mW
External source power	2.7 W

the cylindrical model, creating the largest difference in source power achievable while normalizing irradiance to the ANSI standard. The external source power becomes 1000× greater than the internal power. The corresponding average fluence rates for external illumination (Table 5) become roughly an order of magnitude higher than for internal illumination. However, as explained below, experimental limitations do not allow the external source to reach the same irradiance level as the internal source. If operation at the same irradiance levels was possible in the experimental setup, the efficiency rates and spatial distribution of light in the lung would remain poor for external illumination.

Specifically for our application, the external source in the whole animal imaging system at the highest setting is roughly 3 to 8 mW, depending on the spectral filtering. This power is evenly distributed over the entire platform at the base of the chamber (~3500 cm^2)[53] and not over the surface of the animal (~400 mm^2). A higher, yet still very safe, irradiance is achieved with the internal source, which operates at ~0.4 to 1.3 mW. This power is incident on a much smaller area than the external source (0.342 mm^2). Using these values, the experimental irradiance ranges from 9 to 24 $\mu W/mm^2$ for the external source and 1200 to 3800 $\mu W/mm^2$ for the internal source, which is between two and three orders of magnitude difference. As stated earlier, the external source power would have to be about 1000× greater than the internal source to achieve the same irradiance. The comparisons drawn in this paper with the two sources both at 1 mW of power are therefore on the appropriate scale for comparing with experimental data.

4.2 *External Illumination and Mouse Position*

Previous animal experiments show a difference in fluorescence detected in different positions of the mouse in the imaging system, specifically in positioning the mouse ventrally or dorsally within the imaging system.[18] Simulations of dorsal and ventral external illumination show that positioning the mouse dorsally with respect to the external imaging source more effectively couples the excitation light into the lung, supporting previous experimental results. The main explanation for this is the location of the heart within the thoracic cavity. At visible wavelengths, the heart and blood are highly absorbing. In the NIR, the heart does not absorb as much light, but it increases the path length that a photon must travel to arrive at the lung, increasing the likelihood that a photon is absorbed or scattered away from the lung. This model demonstrates the effect of the heart on ventral illumination. The simplification of all other biological tissues into one layer is an approximation, but it is anatomically similar from either side of the animal, incorporating skin, other soft tissue, and rib cage (not included in this model), which are all present both ventrally and dorsally.

4.3 *Optimal Illumination of the Mouse Lung*

The goal of the internal illumination source is to better couple excitation light into the tissue of interest that may contain a fluorescent marker. For the specific application of detecting bacteria within the lung, there is no *a priori* knowledge about the location of the bacteria within the lungs of a given mouse. Diffuse, widespread illumination would therefore be an ideal tool for effectively detecting low numbers of bacteria within the lung. By simulating the physiology of the mouse and the optical system, the efficacy of different sources, different protocols, and even different animal positions can be analyzed without performing a large number of animal imaging experiments.

The fiber diffuser was determined to be a poor illumination source in the trachea due to its low efficiency of coupling light into the lung. While it did show a more uniform illumination of the lungs (data not shown), the light coupled into the lung was much lower than the current ME design. It is possible that a single lobe of the lung could be illuminated well by the fiber diffuser if the diffuser could be positioned deeper into the airway. In the current model, most of the power that was emitted along the length of the diffuser escaped through the trachea and into the surrounding tissue without ever reaching the lung. While positioning the diffuser deeper in the lung could remedy this, the current ME does not have the capability to steer the tip in the airway. The current fiber bundle diameter (0.66 mm) is close to the inner diameter of the trachea (~1.3 mm), so there is also an anatomical size limitation with going much deeper in the mouse lung with these sources. Given a larger animal model, such experiments and corresponding simulations might be feasible.

The most effective manipulation of the internal illumination source was the placement of the source within the trachea. While the simulations indicate an enhanced illumination of the lung model, the effect of source placement *in vivo* may vary among animals. The airway will follow similar branching patterns in every mouse, but variability in animal size and lung development will likely hinder the reproduction of the simulation results *in vivo*. A change in the experimental protocol would still be recommended, as a small distance between the light source and tracheal bifurcation should show an increase in delivery of light to the lungs in any animal.

While changing the divergence angle of the source did not show the greatest increase in source efficiency or average fluence rate in the lung, it may be the best way to reproducibly enhance the illumination of the lung in animal experiments. An increase ($p \ll 0.0001$) in average fluence rate and coupling efficiency into the lung was found with the 40 deg half angle source relative to the current 20.5 deg half angle divergence of the microendoscope source. An increase of average fluence

rate in the lung is expected to be more consistent with this change to the optical system than with an optimized experimental protocol regarding source placement.

5 Summary

A 3-D Monte Carlo model of the mouse lung and torso has been developed to analyze the capabilities of different excitation sources to illuminate the lung. The model approximates the physiology of the mouse torso and can simulate both internal and external light sources. By isolating the lung tissue, the radiative transport within the lung has been compared across internal and external sources and across modifications to the internal source. By optimizing the illumination of the lung with the computational model, the system will ideally be well suited to detecting infection of a range of bacterial loads, regardless of the localization of the infection within the lung. The results of these simulations do help to explain the two- to threefold improvement of the detection threshold of bacterial load in the previous experiments.[17,18] However, a full analysis of the limitations of fluorescence detection is planned by extrapolating this model to include fluorescent bacteria to estimate the effect of optimal illumination on fluorescence detection in various infection scenarios. The model indicates that the system is very sensitive to the placement of the internal source, a variable which is not easily controlled experimentally, and could change significantly among animals. However, slightly improved illumination of the lung can be achieved by increasing the divergence of the internal source, which is an instrumentation change that can more readily be applied to the system. Overall, the validated model approximates the physiology well and can be used as a tool to help optimize the imaging system and animal imaging protocol for future experiments.

Disclosures

The authors have no relevant financial interests in this article and no potential conflicts of interest to disclose.

Acknowledgments

This work was supported by the National Science Foundation CAREER award no. CBET-1254767 and the National Institute of Allergy and Infectious Diseases grant no. R01AI104960.

References

1. World Health Organization, "Global tuberculosis report 2016," WHO/HTM/TB/2016.13, WHO Press, Geneva (2016).
2. M. Brown et al., "Prospective study of sputum induction, gastric washing, and bronchoalveolar lavage for the diagnosis of pulmonary tuberculosis in patients who are unable to expectorate," *Clin. Infect. Dis.* **44**(11), 1415–1420 (2007).
3. C. T. Sreeramareddy et al., "Time delays in diagnosis of pulmonary tuberculosis: a systematic review of literature," *BMC Infect. Dis.* **9**, 91 (2009).
4. R. P. Tiwari et al., "Modern approaches to a rapid diagnosis of tuberculosis: promises and challenges ahead," *Tuberculosis* **87**(3), 193–201 (2007).
5. C. J. Cambier, S. Falkow, and L. Ramakrishnan, "Host evasion and exploitation schemes of mycobacterium tuberculosis," *Cell* **159**(7), 1497–1509 (2014).
6. J. A. M. Langermans et al., "Divergent effect of bacillus Calmette–Guérin (BCG) vaccination on Mycobacterium tuberculosis infection in highly related macaque species: implications for primate models in tuberculosis vaccine research," *Proc. Natl. Acad. Sci. U. S. A.* **98**(20), 11497–11502 (2001).
7. D. N. McMurray, "Guinea pig model of tuberculosis," in *Tuberculosis*, B. Bloom, Ed., pp. 135–147, ASM Press, Washington, DC (1994).
8. I. M. Orme and F. M. Collins, "Mouse model of tuberculosis," in *Tuberculosis*, B. Bloom, Ed., pp. 113–134, ASM Press, Washington, DC (1994).
9. K. Andries, T. Gevers, and N. Lounis, "Bactericidal potencies of new regimens are not predictive of their sterilizing potencies in a murine model of tuberculosis," *Antimicrob. Agents Chemother.* **54**(11), 4540–4544 (2010).
10. W. P. Gill et al., "A replication clock for Mycobacterium tuberculosis," *Nat. Med.* **15**(2), 211–214 (2009).
11. M. Baker, "Whole-animal imaging: the whole picture," *Nature* **463**(7283), 977–980 (2010).
12. V. E. Calderon et al., "A humanized mouse model of tuberculosis," *PLoS ONE* **8**(5), e63331 (2013).
13. Y. Kong et al., "Application of optical imaging to study of extrapulmonary spread by tuberculosis," *Tuberculosis* **89**(Suppl. 1), S15–S17 (2009).
14. H.-J. Yang et al., "Real-time imaging of Mycobacterium tuberculosis using a novel near-infrared fluorescent substrate," *J. Infect. Dis.* **215**(3), 405–414 (2016).
15. Y. Kong et al., "Whole-body imaging of infection using fluorescence," *Curr. Protoc. Microbiol.* **21**(2C.3), 2C.3.1–2C.3.21 (2011).
16. E. A. Nardell, "Transmission and institutional infection control of tuberculosis," *Cold Spring Harbor Perspect. Med.* **6**(2), a018192 (2016).
17. F. Nooshabadi et al., "Intravital fluorescence excitation in whole-animal optical imaging," *PLoS ONE* **11**(2), e0149932 (2016).
18. F. Nooshabadi et al., "Intravital excitation increases detection sensitivity for pulmonary tuberculosis by whole-body imaging with β-lactamase reporter enzyme fluorescence," *J. Biophotonics* **10**(6–7), 821–829 (2017).
19. C. Zhu and Q. Liu, "Review of Monte Carlo modeling of light transport in tissues," *J. Biomed. Opt.* **18**(5), 050902 (2013).
20. L. Wang, S. L. Jacques, and L. Zheng, "MCML—Monte Carlo modeling of light transport in multi-layered tissues," *Comput. Meth. Prog. Bio.* **47**(2), 131–146 (1995).
21. D. A. Boas et al., "Three dimensional Monte Carlo code for photon migration through complex heterogeneous media including the adult human head," *Opt. Express* **10**(3), 159–170 (2002).
22. Q. Fang, "Mesh-based Monte Carlo method using fast ray-tracing in Plücker coordinates," *Biomed. Opt. Express* **1**(1), 165–175 (2010).
23. H. Li et al., "A mouse optical simulation environment (MOSE) to investigate bioluminescent phenomena in the living mouse with the Monte Carlo method," *Acad. Radiol.* **11**(9), 1029–1038 (2004).
24. S. Ren et al., "Molecular optical simulation environment (MOSE): a platform for the simulation of light propagation in turbid media," *PLoS ONE* **8**(4), e61304 (2013).
25. D. J. Smithies and P. H. Butler, "Modelling the distribution of laser light in port-wine stains with the Monte Carlo method," *Phys. Med. Biol.* **40**(5), 701–731 (1995).
26. T. J. Pfefer et al., "A three-dimensional modular adaptable grid numerical model for light propagation during laser irradiation of skin tissue," *IEEE J. Sel. Top. Quantum Electron.* **2**(4), 934–942 (1996).
27. H. Funamizu et al., "Simulation of spectral reflectances in human skin tissue using ray tracing and GPU-based Monte Carlo method," *Opt. Rev.* **21**(3), 359–363 (2014).
28. C.-Y. Huang et al., "Novel wearable and wireless ring-type pulse oximeter with multi-detectors," *Sensors* **14**(9), 17586–17599 (2014).
29. S. A. Prahl, "Optical property measurements using the inverse adding-doubling program," January 1999, http://citeseerx.ist.psu.edu/viewdoc/download?doi=10.1.1.202.3942&rep=rep1&type=pdf (15 March 2018).
30. J. Beek et al., "The optical properties of lung as a function of respiration," *Phys. Med. Biol.* **42**(11), 2263–2272 (1997).
31. V. Tuchin, *Tissue Optics: Light Scattering Methods and Instruments for Medical Diagnostics*, 3rd ed., SPIE Press, Bellingham, Washington (2015).
32. W. Hwang et al., "In vitro study of transcatheter delivery of a shape memory polymer foam embolic device for treating cerebral aneurysms," *J. Med. Devices* **7**(2), 020932 (2013).
33. P. Diep et al., "Three-dimensional printed optical phantoms with customized absorption and scattering properties," *Biomed. Opt. Express* **6**(11), 4212–4220 (2015).
34. J. Wang et al., "Three-dimensional printing of tissue phantoms for biophotonic imaging," *Opt. Lett.* **39**(10), 3010–3013 (2014).

35. G. T. Smith et al., "Multimodal 3D cancer-mimicking optical phantom," *Biomed. Opt. Express* **7**(2), 648–662 (2016).
36. M. S. Durkee et al., "Fabrication and characterization of optical tissue phantoms containing macrostructure," *J. Visualized Exp.* **2018**(132), e57031 (2018).
37. N. Mufti et al., "Fiber optic microendoscopy for preclinical study of bacterial infection dynamics," *Biomed. Opt. Express* **2**(5), 1121–1134 (2011).
38. N. L. Ford et al., "Optimization of a retrospective technique for respiratory-gated high speed micro-CT of free-breathing rodents," *Phys. Med. Biol.* **52**(19), 5749–5769 (2007).
39. X. Artaechevarria et al., "Airway segmentation and analysis for the study of mouse models of lung disease using micro-CT," *Phys. Med. Biol.* **54**(22), 7009–7024 (2009).
40. E. Namati et al., "Longitudinal assessment of lung cancer progression in the mouse using in vivo micro-CT imaging," *Med. Phys.* **37**(9), 4793–4805 (2010).
41. W. Mitzner, R. Brown, and W. Lee, "In vivo measurement of lung volumes in mice," *Physiol. Genomics* **4**(3), 215–221 (2001).
42. C. G. Tankersley, R. Rabold, and W. Mitzner, "Differential lung mechanics are genetically determined in inbred murine strains," *J. Appl. Physiol.* **86**(6), 1764–1769 (1999).
43. C. Irvin and J. Bates, "Measuring the lung function in the mouse: the challenge of size," *Respir. Res.* **4**(1), 1–9 (2003).
44. L. Bi et al., "Single-scattering properties of triaxial ellipsoidal particles for a size parameter range from the Rayleigh to geometric-optics regimes," *Appl. Opt.* **48**(1), 114–126 (2009).
45. M. U. Vera, A. Saint-Jalmes, and D. J. Durian, "Scattering optics of foam," *Appl. Opt.* **40**(24), 4210–4214 (2001).
46. D. J. Durian, D. A. Weitz, and D. J. Pine, "Multiple light-scattering probes of foam structure and dynamics," *Science* **252**(5006), 686–688 (1991).
47. L. Knudsen et al., "Assessment of air space size characteristics by intercept (chord) measurement: an accurate and efficient stereological approach," *J. Appl. Physiol.* **108**(2), 412–421 (2010).
48. C. G. Tankersley, R. S. Fitzgerald, and S. R. Kleeberger, "Differential control of ventilation among inbred strains of mice," *Am. J. Physiol.* **267**(5), R1371–R1377 (1994).
49. E. Osmanagic et al., "Quantitative assessment of lung microstructure in healthy mice using an MR-based lung morphometry technique," *J. Appl. Physiol.* **109**(6), 1592–1599 (2010).
50. S. E. Soutiere, C. G. Tankersley, and W. Mitzner, "Differences in alveolar size in inbred mouse strains," *Respir. Physiol. Neurobiol.* **140**(3), 283–291 (2004).
51. "LightTools biological materials library," Synopsys, Inc. (2014).
52. W. Small et al., "Fabrication and characterization of cylindrical light diffusers comprised of shape memory polymer," *J. Biomed. Opt.* **13**(2), 024018 (2008).
53. "IVIS lumina system manual," Xenogen Corporation (2006).

Biographies for the authors are not available.